

There are important differences between the latitudinal structure of trends for the second half of the 20th century and for the 21st century (2000–2014) (Fig. 3). For example, the Arctic latitudes have shown strong warming trends both over the land and ocean since 2000, but during the latter half of the 20th century, the ocean trends in this area are near zero. The longer-term 50-year trend has more consistency in the rates of warming across all latitudes, and this is even more evident over the full period of record back to 1880 (fig. S1). There is a distinct Northern Hemisphere mid-latitude cooling in LST during the 21st century, which is also showing up in cooling of the cold extremes, as reported for the extreme minimum temperatures in this zone in (27). Atmospheric teleconnections and regional forcings could be relevant in understanding these short time-scale zonal trends. It is evident that in most latitude bands, the global trends in the past 15 years are comparable with trends in the preceding 50 years.

Last, we considered the impact of larger warming rates in high latitudes (24) on the overall global trend. To estimate the magnitude of the additional warming, we applied large-area interpolation over the poles using the limited observational data available. Results indicate that, indeed, additional global warming of a few hundredths of a degree Celsius per decade over the 21st century is evident (Fig. 1), providing further evidence against the notion of a recent warming “hiatus” (supplementary materials).

Newly corrected and updated global surface temperature data from NOAA’s NCEI do not support the notion of a global warming “hiatus.” As shown in Fig. 1, there is no discernable (statistical or otherwise) decrease in the rate of warming between the second half of the 20th century and the first 15 years of the 21st century. Our new analysis now shows that the trend over the period 1950–1999, a time widely agreed as having significant anthropogenic global warming (1), is $0.113^{\circ}\text{C decade}^{-1}$, which is virtually indistinguishable from the trend over the period 2000–2014 ($0.116^{\circ}\text{C decade}^{-1}$). Even starting a trend calculation with 1998, the extremely warm El Niño year that is often used as the beginning of the “hiatus,” our global temperature trend (1998–2014) is $0.106^{\circ}\text{C decade}^{-1}$ —and we know that is an underestimate because of incomplete coverage over the Arctic. Indeed, according to our new analysis, the IPCC’s (1) statement of 2 years ago—that the global surface temperature “has shown a much smaller increasing linear trend over the past 15 years than over the past 30 to 60 years”—is no longer valid.

REFERENCES AND NOTES

- IPCC, *Climate Change 2013: The Physical Science Basis. Contribution of Working Group I to the Fifth Assessment Report of the Intergovernmental Panel on Climate Change*, T. F. Stocker, D. Qin, G.-K. Plattner, M. Tignor, S.K. Allen, J. Boschung, A. Nauels, Y. Xia, V. Bex, P.M. Midgley, Eds. (Cambridge Univ. Press, Cambridge, 2013).
- G. A. Meehl, H. Teng, J. M. Arblaster, *Nature Clim. Change* **4**, 898–902 (2014).
- G. A. Meehl, A. Hu, J. M. Arblaster, J. Fasullo, K. E. Trenberth, *J. Clim.* **26**, 7298–7310 (2013).
- Y. Kosaka, S.-P. Xie, *Nature* **501**, 403–407 (2013).
- M. H. England et al., *Nature Clim. Change* **4**, 222–227 (2014).
- B. D. Santer et al., *Nat. Geosci.* **7**, 185–189 (2014).
- G. A. Schmidt, D. T. Shindell, K. Tsigaridis, *Nat. Geosci.* **7**, 158–160 (2014).
- J. Tollefson, *Nature* **505**, 276–278 (2014).
- M. Watanabe et al., *Geophys. Res. Lett.* **40**, 3175–3179 (2013).
- J. C. Fyfe, N. P. Gillett, *Nature Clim. Change* **4**, 150–151 (2014).
- K. E. Trenberth, J. T. Fasullo, M. A. Balmaseda, *J. Clim.* **27**, 3129–3144 (2014).
- H. Ding, R. J. Greatbatch, M. Latif, W. Park, R. Gerdes, *J. Clim.* **26**, 7650–7661 (2013).
- B. Huang et al., *J. Clim.* **28**, 911–930 (2015).
- J. J. Rennie et al., *Geosci. Data J.* **1**, 75–102 (2014).
- E. C. Kent, J. J. Kennedy, D. I. Berry, R. O. Smith, *Clim. Change* **1**, 718–728 (2010).
- R. W. Reynolds, N. A. Rayner, T. M. Smith, D. C. Stokes, W. Wang, *J. Clim.* **15**, 1609–1625 (2002).
- R. W. Reynolds, D. B. Chelton, *J. Clim.* **23**, 3545–3562 (2010).
- J. J. Kennedy, N. A. Rayner, R. O. Smith, D. E. Parker, M. Saunby, *J. Geophys. Res. Atmos.* **116** (D14), D14104 (2011).
- J. H. Lawrimore, J. J. Rennie, P. W. Thorne, *Eos* **94**, 61 (2014).
- M. J. Menne, I. Durre, R. S. Vose, B. E. Gleason, T. G. Houston, *J. Atmos. Ocean. Technol.* **29**, 897–910 (2012).
- M. J. Menne, C. N. Williams Jr., *J. Clim.* **22**, 1700–1717 (2009).
- J. H. Lawrimore et al., *J. Geophys. Res.* **116** (D19), D19121 (2011).
- C. N. Williams, M. J. Menne, P. W. Thorne, *J. Geophys. Res.* **117** (D5), D05116 (2012).
- K. Cowtan, R. G. Way, *Q. J. Roy. Met. Soc.* **140**, 1935–1944 (2014).
- B. Santer et al., *Int. J. Climatol.* **28**, 1703–1722 (2008).
- T. M. Smith, R. W. Reynolds, *J. Clim.* **16**, 1495–1510 (2003).
- J. Sillman, M. G. Donat, J. C. Fyfe, F. W. Zwiers, *Environ. Res. Lett.* **9**, 064023 (2014).

ACKNOWLEDGMENTS

We thank the many scientists at NCEI and at other institutions who routinely collect, archive, quality control, and provide access to the many complex data streams that go into the computation of the global surface temperature. In particular, we thank T. Boyer, B. Gleason, J. Matthews, J. Rennie, and C. Williams for their contributions to this analysis. We also thank J. Meehl and P. Duffy for constructive comments on an early version of this manuscript.

SUPPLEMENTARY MATERIALS

www.sciencemag.org/content/348/6242/1469/suppl/DC1
Materials and Methods
Fig. S1
Table S1
References (28–38)

23 December 2014; accepted 21 May 2015
Published online 4 June 2015;
10.1126/science.aaa5632

BRAIN CIRCUITS

A parvalbumin-positive excitatory visual pathway to trigger fear responses in mice

Congping Shang,^{1,2} Zhihui Liu,¹ Zijun Chen,^{1,2} Yingchao Shi,^{1,2} Qian Wang,¹ Su Liu,¹ Dapeng Li,¹ Peng Cao^{1*}

The fear responses to environmental threats play a fundamental role in survival. Little is known about the neural circuits specifically processing threat-relevant sensory information in the mammalian brain. We identified parvalbumin-positive (PV⁺) excitatory projection neurons in mouse superior colliculus (SC) as a key neuronal subtype for detecting looming objects and triggering fear responses. These neurons, distributed predominantly in the superficial SC, divergently projected to different brain areas, including the parabrachial nucleus (PBN), an intermediate station leading to the amygdala. Activation of the PV⁺ SC-PBN pathway triggered fear responses, induced conditioned aversion, and caused depression-related behaviors. Approximately 20% of mice subjected to the fear-conditioning paradigm developed a generalized fear memory.

Environmental threats are detected by different sensory organs projecting to central brain areas to trigger fear responses (1, 2). The superior colliculus (SC) is a retinal recipient structure (3, 4) composed of different neuronal subtypes (5, 6), including parvalbumin-positive (PV⁺), somatostatin-positive (SST⁺), and vasoactive intestinal peptide-positive (VIP⁺) neurons (Fig. 1A and fig. S1). In addition to mediating orienting responses (7), the SC contributes to avoidance and defense-like behaviors (8–11).

With an optogenetic approach (12–14), we found that activation of neurons expressing channelrhodopsin-2 (ChR2) in mouse SC triggered freezing that lasted 52.8 ± 5.3 s ($n = 5$ mice) (movie S1). This prompted us to systematically identify the key neuronal subtypes underlying this behavior.

By crossing Ai32 (15) with different Cre lines (Fig. 1B) (16, 17), we expressed ChR2-enhanced yellow fluorescent protein (EYFP) in specific neuronal subtypes in the SC (Fig. 1C and fig. S1) and optogenetically elicited spikes in acute slices (Fig. 1D and fig. S1). Activation of SC PV⁺ neurons, but not SST⁺ or VIP⁺ neurons, triggered impulsive escaping (1.18 ± 0.09 s) followed by long-lasting freezing (46.4 ± 2.8 s) (Fig. 1, E to G; fig. S1; and movie S2). To avoid activation of PV⁺ retinal

¹State Key Laboratory of Brain and Cognitive Sciences, Institute of Biophysics, Chinese Academy of Sciences, Beijing 100101, China. ²University of Chinese Academy of Sciences, Beijing 100049, China.

*Corresponding author. E-mail: pcao@ibp.ac.cn

ganglion cells (RGCs) (18) by ferrule light, we injected adeno-associated virus (AAV) expressing double-floxed ChR2-mCherry (12) into the SC of *PV-ires-Cre* mice, resulting in specific expression of ChR2-mCherry in SC PV⁺ neurons but not in PV⁺ RGCs (Fig. 2A and fig. S2). The light triggered spikes from ChR2-mCherry-positive neurons in SC slices (Fig. 2B and fig. S2), elicited a similar stereotyped locomotor pattern (fig. S2 and movie S3), and increased the heart rate and plasma corticosterone levels that were not observed in mice with SC PV⁺ neurons expressing mCherry (Fig. 2, C and D).

When facing threats, animals can either fight or flee. To test whether SC PV⁺ neurons were involved in this behavioral dichotomy, we measured the durations of light-induced escaping (E) and freezing (F) and calculated their ratio

(E/F ratio). We conducted a series of tests spanning 5 days (table S1). First, light stimulations with higher intensity or longer duration enhanced E/F ratios in the same male mice by prolonging escaping more strongly than freezing (Fig. 2, E and F). Second, light stimulations with higher frequency but similar total illumination time prolonged escaping and freezing proportionally (Fig. 2G). Third, both responses showed strong adaptation to repetitive light stimulations (every 5 min), with no significant change in E/F ratios across each stimulation (Fig. 2H). Finally, the same light stimulations elicited longer escaping and shorter freezing in female versus male mice, resulting in higher E/F ratios in females (Fig. 2I). The origin of these sexually dimorphic behaviors was further examined (supplementary text).

We next characterized the morphological and physiological properties of SC PV⁺ neurons. They were predominantly but not exclusively distributed in the superficial gray (SuG) layer of the SC (Fig. 3A and fig. S3). Whole-cell recording of tdTomato-expressing PV⁺ neurons in SC slices from *PV-ires-Cre; Ai9* mice (19) demonstrated that, distinct from V1 PV⁺ interneurons with slow frequency adaptation (20), the SuG PV⁺ neurons responded to depolarizing currents in a faster adaptation mode (Figs. 3, C and D, and fig. S3). SuG PV⁺ neurons labeled with neurobiotin had parallel dendrites extending to the SC surface, presumably receiving inputs from RGCs (Fig. 3B and fig. S3). The postsynaptic currents from PV-negative neurons induced by optogenetic activation of PV⁺ neurons expressing ChR2-mCherry were blocked by

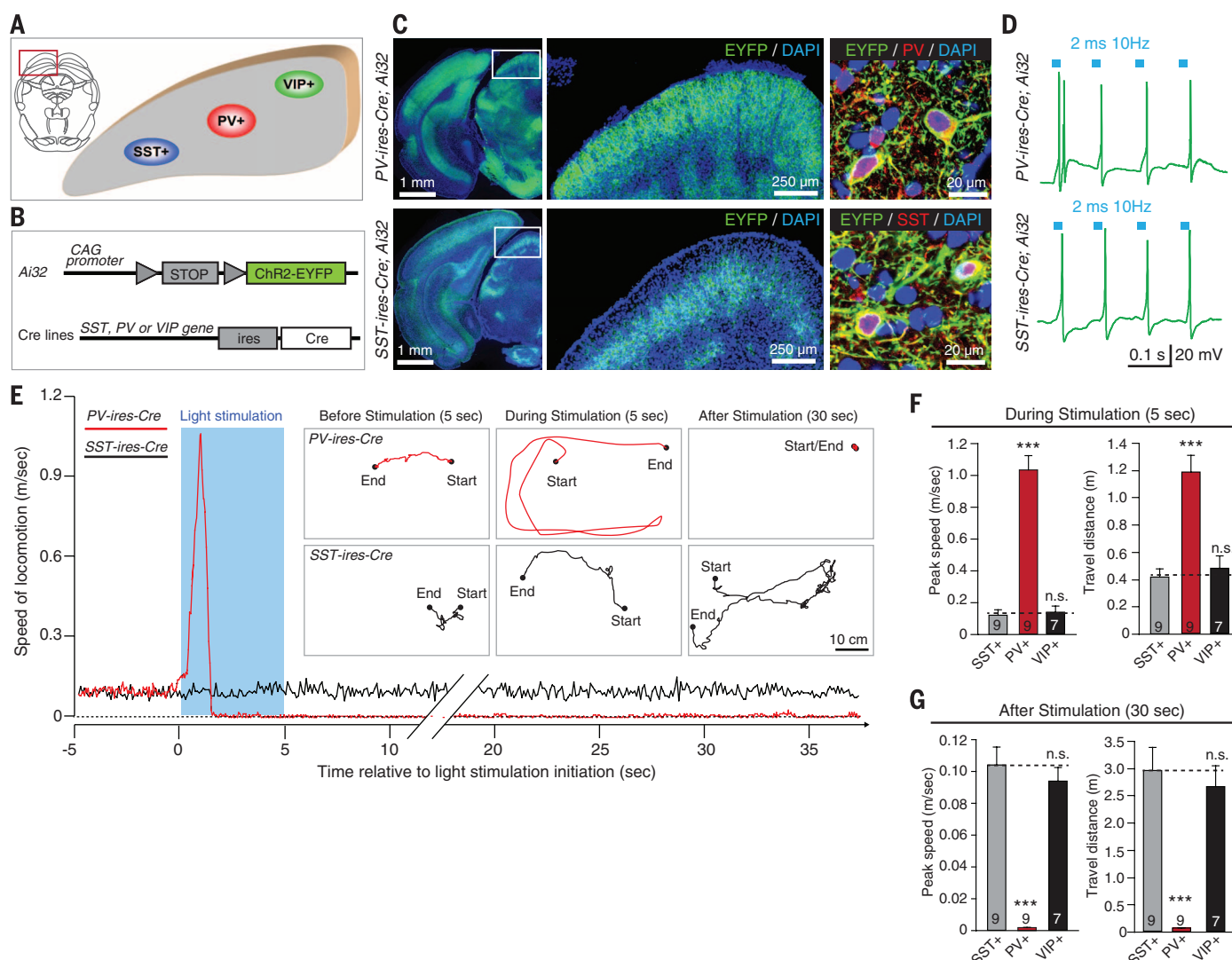


Fig. 1. Neuronal subtypes in the SC to trigger fear responses. (A) Diagram of different neuronal subtypes in the SC. (B) *Ai32* mice were crossed with different Cre lines. (C) Coronal micrographs showing ChR2-EYFP expressed in specific neuronal subtypes. DAPI, 4',6-diamidino-2-phenylindole. (D) Light-induced spikes from ChR2-EYFP⁺ neurons in acute slices. (E) Instantaneous locomotion speed before, during, and after light stimulation. (Inset)

Locomotion trails from example mice. (F and G) Analyses of peak speed and travel distance during and after light stimulation. Data in (F) and (G) are means \pm SEM (error bars); numbers of mice are in bars. Statistical analysis is *t* test (***) $P < 0.001$; n.s. $P > 0.1$). Dashed lines in (F) and (G) indicate the control levels measured from behaviors after SC SST⁺ neuron activation.

D(-)-2-amino-5-phosphonopentanoic acid (APV) and 6-cyano-7-nitroquinoxaline-2,3-dione (CNQX), but not by picrotoxin (Fig. 3, E and F, and fig. S3), suggesting that these neurons were glutamatergic but did not release γ -aminobutyric acid. The SC PV⁺ neurons in intermediate and deep layers of the SC were examined (supplementary text).

To test whether SC PV⁺ neurons were involved in detecting collision threats in the visual field (21–23), we displayed a virtual soccer ball moving in controlled velocities and directions to the anaesthetized mice (Fig. 3J and fig. S4). The single-unit activity recorded with optrodes was quantitatively identified (24, 25) as putative SC PV⁺ neurons expressing ChR2-mCherry (Fig. 3, G to I). These putative PV⁺ neurons ($n = 9$ cells) were strongly activated by the ball moving toward the animal but not by the motion in the other

five directions (Fig. 3K). The response onset time before collision depended on the size and velocity of the ball (Fig. 3L) and was linearly correlated with the square root of the diameter/velocity (Fig. 3M). The response peak was close to the time to collision and was independent of the size and velocity of the soccer ball (Fig. 3N). In freely behaving mice, the escaping triggered by SC PV⁺ neuron activation pointed to the side of the SC receiving light stimulation (movie S4).

We then determined the circuit mechanism underlying the fear responses mediated by SC PV⁺ neurons. By injecting AAV expressing double-floxed monomeric green fluorescent protein (mGFP) into the SC of *PV-ires-Cre* mice, we specifically labeled SC PV⁺ neurons (Fig. 4B and figs. S5 and S6) and observed axon terminals in the parabrachial nucleus (PBN), the pontine

nucleus (Pn), and the dorsal lateral geniculate nucleus (DLGN) (Fig. 4, A and C). These projections were confirmed by retrograde tracing with cholera toxin B with Alexa Fluor-594 (CTB-594). CTB-594 injection into the PBN (Fig. 4D) retrogradely labeled SC neurons predominantly in the ipsilateral SuG layer (Fig. 4E and fig. S7). A considerable proportion of CTB-labeled SC neurons (SC-PBGN: $52 \pm 4.3\%$; SC-Pn: $31 \pm 4.5\%$; SC-DLGN: $33 \pm 3.8\%$, $n = 3$ mice) were positive for PV (Fig. 4F and fig. S7).

To determine which of these parallel projections (26) participated in the fear responses, we injected AAV expressing double-floxed ChR2-mCherry into the SC and implanted optic fibers in the PBGN or Pn (Fig. 4G) to locally stimulate the ChR2-mCherry-positive axon terminals. Activation of the PV⁺ SC-PBGN pathway, but not the PV⁺ SC-Pn pathway, triggered the stereotyped

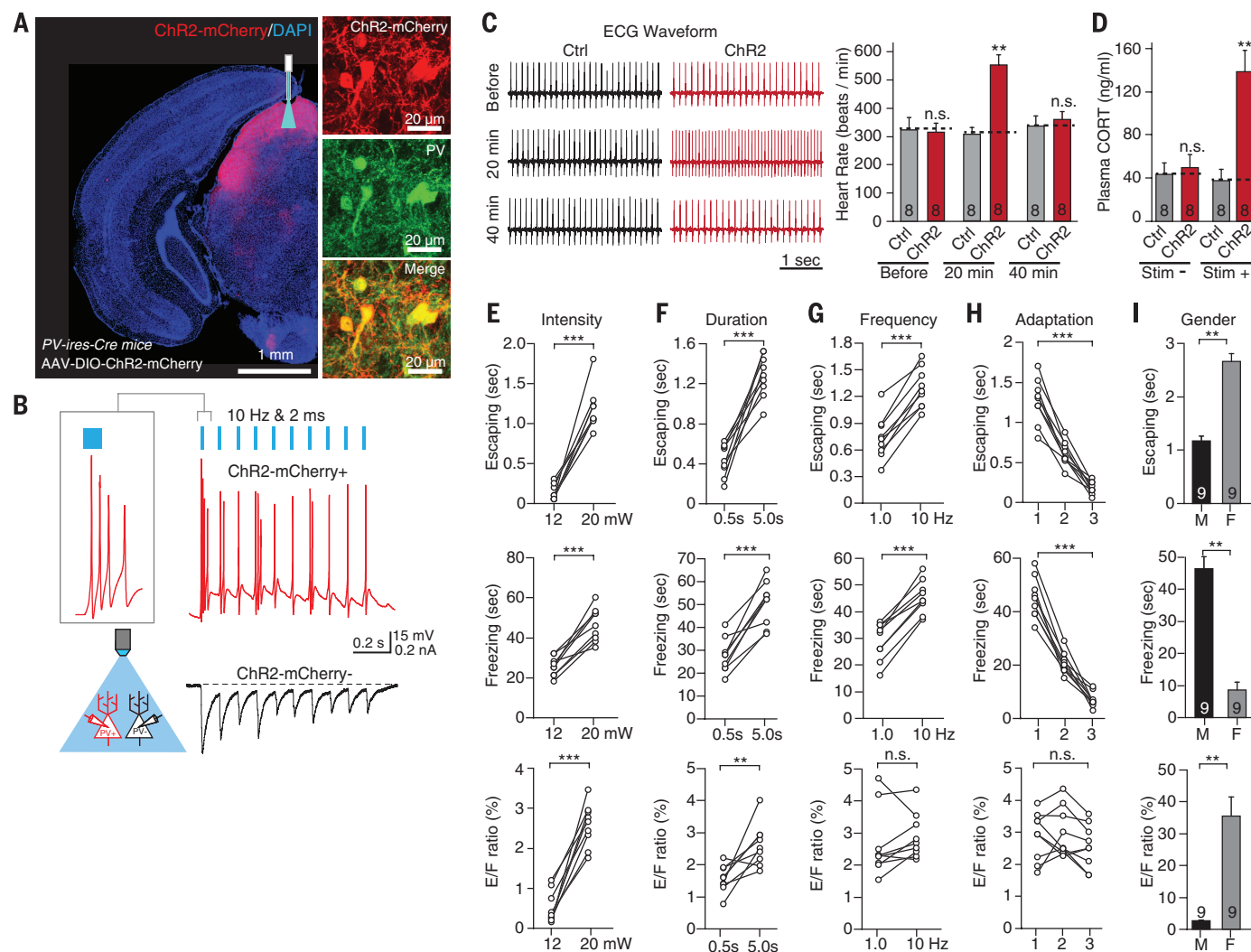


Fig. 2. Specific activation of SC PV⁺ neurons induced fear responses.

(A) Specific expression of ChR2-mCherry in SC PV⁺ neurons of *PV-ires-Cre* mice. (B) The light-pulse train triggered spikes (red) from ChR2-mCherry-positive neurons and postsynaptic currents (black) from adjacent ChR2-mCherry-negative neurons. (C) Electrocardiographic traces and heart rate analyses from the anaesthetized mice before and after light stimulation. Ctrl, control. (D) Analyses of plasma corticosterone concentration in

response to light stimulation. (E to I) Durations of escaping, freezing, and E/F ratios, were plotted as functions of stimulation intensity, duration, frequency, repetition, and sex in mice with SC PV⁺ neurons expressing ChR2-mCherry. Data in (C) to (I) are means \pm SEM (error bars); numbers of mice are in bars. Statistical analysis is *t* test (*** $P < 0.001$; ** $P < 0.01$; n.s. $P > 0.1$). Dashed lines indicate the levels measured from control mice. M, male; F, female.

escaping-freezing locomotor pattern (Fig. 4, H to J; fig. S9, and movie S5). We examined whether PBGN projected to the amygdala by anterograde and retrograde tracings. Local injection of AAV-SynaptoTag (27) in the PBGN and its adjacent

region strongly labeled axon terminals positive for synaptobrevin-2-EGFP in the central amygdaloid nucleus (28, 29), whereas CTB-594 injection in the amygdala retrogradely labeled neurons in the PBGN (fig. S8). Finally, the relation between

PV⁺ SC-PBGN pathway activation and the affective state of mice was explored (supplementary text and figs. S10 to S12). Taken together, these data revealed a PV⁺ excitatory visual pathway to trigger stereotyped fear responses in mice.

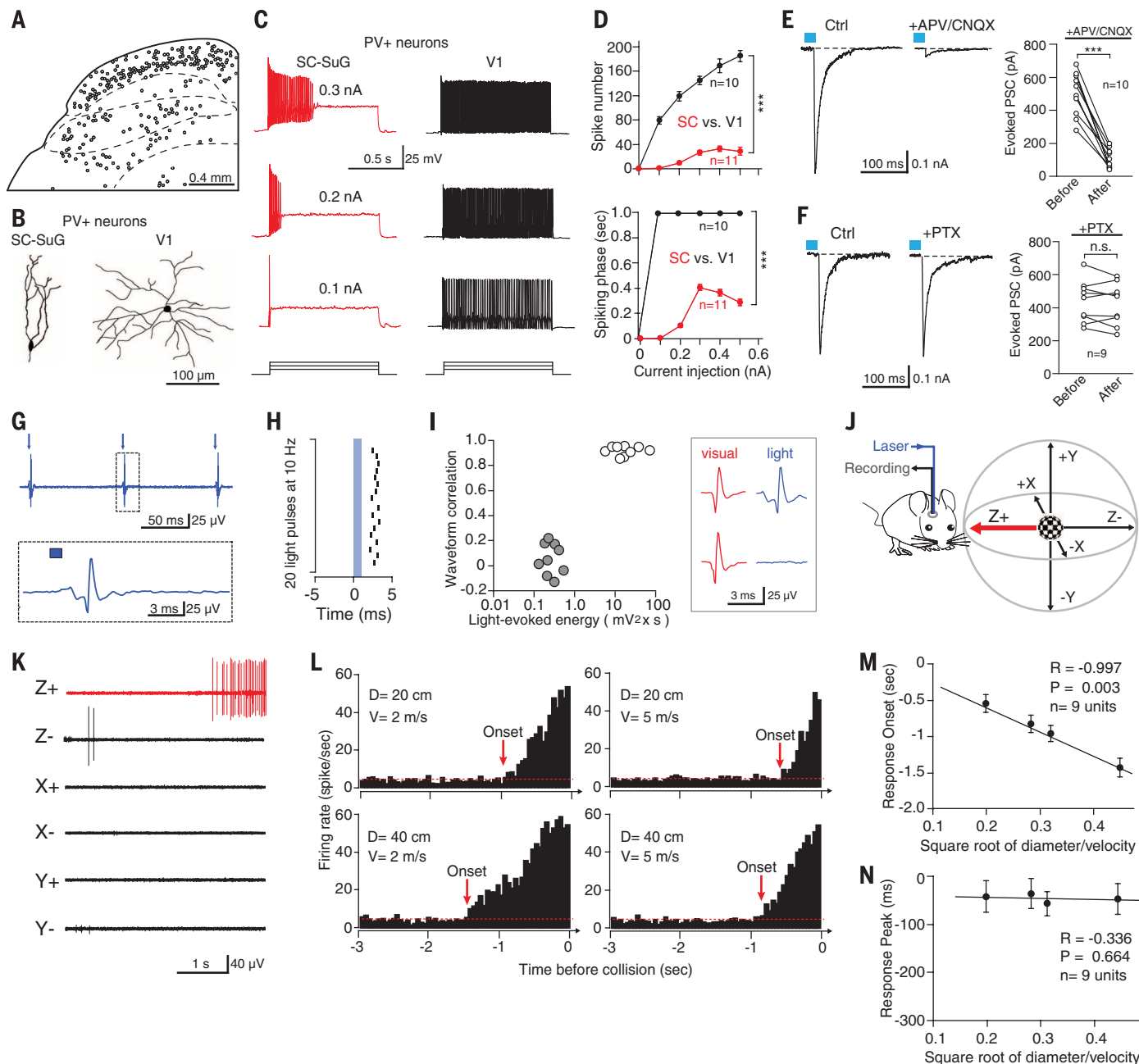


Fig. 3. Morphological and physiological properties of SC PV⁺ neurons.

(**A**) Layer-specific distribution of SC PV⁺ neurons. (**B**) Neurobiotin-labeled PV⁺ neurons in the SC SuG layer and V1. (**C**) Spike firings of PV⁺ neurons in the SC and V1 to depolarizing currents. (**D**) Analyses of spike number and spiking phase as a function of current intensity. *n*, number of cells. (**E** and **F**) Effects of CNQX (20 μ M)/APV (50 μ M) (**E**) and picrotoxin (50 μ M) (**F**) on the postsynaptic currents (PSC) induced by light stimulation. *n*, number of cells. (**G**) Single-unit activity recorded from a putative SC PV⁺ neuron triggered by light pulses (arrows, 1 ms at 10 Hz). (**H**) Raster plot showing the latency of light-evoked spikes relative to the light pulses (0 ms). (**I**) Distributional plot (left) and example spikes (right) evoked by visual stimuli and light showing quantitative identification of PV-positive and PV-negative units based on the

waveform correlation and energy of light-evoked spikes. (**J**) A virtual soccer ball flying toward the eye of an anesthetized mouse. (**K**) Example single-unit traces from a putative SC PV⁺ neuron in response to the soccer ball (20 cm in diameter) moving in six directions at 2 m/s. (**L**) Peristimulus time histograms of a PV⁺ neuron to looming stimuli with controlled velocities (V) (2 and 5 m/sec) and diameters (D) (20 and 40 cm). Arrows indicate response onset time. (**M** and **N**) Correlation analyses of response onset time (**M**) and response peak time (**N**) of SC PV⁺ neurons and the square root of diameter/velocity of the looming ball. Data are means \pm SEM (error bars); numbers of cells or units are in graphs. Statistical analyses are *t* test and one-way analysis of variance (****P* < 0.001; n.s. *P* > 0.1). R, correlation coefficient.

Our data lead to the following conclusions. First, the SC PV⁺ neurons form a subcortical visual pathway that transmits threat-relevant visual

information to the amygdala to trigger fear responses. These data, in alliance with earlier studies (18, 30, 31), suggest a “retina-SC-PBGN-amygdala-

hypothalamus” pathway for vision-induced fear responses. Second, the SC PV⁺ neurons in the SuG layer are predominantly glutamatergic

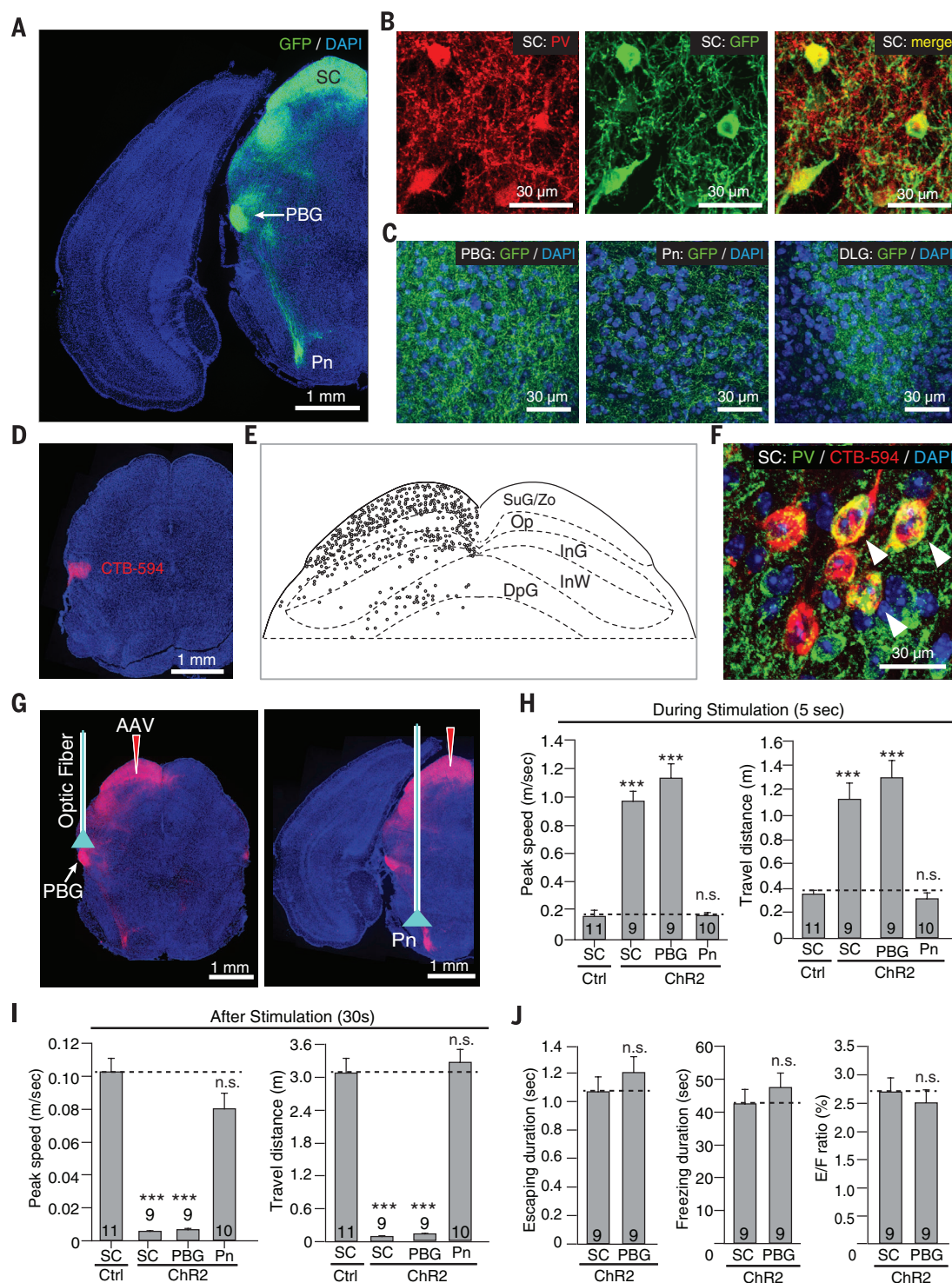


Fig. 4. PV⁺ SC-PBGN pathway mediated fear responses. (A to C) Specific expression of mGFP in SC PV⁺ neurons (B) of PV-ires-Cre mice resulted in labeling of their axon terminals in the PBGN, Pn, and DLGN [(A) and (C)]. (D to F) CTB-594 injected in the PBGN (D) retrogradely labeled cells in the SC (E), a large proportion of which were PV⁺ (denoted by arrowheads) (F). DpG, deep gray layer; InW, intermediate white layer; InG, intermediate gray layer; Op, optic nerve layer; Zo, zonal layer. (G) Diagrams showing the

optic fibers implanted either above the PBGN or the Pn to stimulate ChR2-mCherry-positive axon terminals. (H and I) Locomotion analyses during and after the activation of PV⁺ SC-PBGN and SC-Pn pathways. (J) Analyses of escaping, freezing, and E/F ratio in mice receiving activation of the PV⁺ SC-PBGN pathway and SC PV⁺ neurons. Data in (H) to (J) are means \pm SEM (error bars); numbers of mice are in bars. Statistical analysis is *t* test (****P* < 0.001; n.s. *P* > 0.1).

projection neurons with spiking patterns distinct from those of their counterparts in cortical regions. Thus, this finding broadens the concept of PV⁺ neurons (32) and adds another perspective to understanding their functions. Third, the SC PV⁺ neurons may belong to type-p looming detector, supporting the notion that mathematically defined computational units correspond to specific neuronal subtypes (33).

REFERENCES AND NOTES

1. E. A. Krusemark, W. Li, *J. Neurosci.* **33**, 587–594 (2013).
2. J. P. Johansen, C. K. Cain, L. E. Ostroff, J. E. LeDoux, *Cell* **147**, 509–524 (2011).
3. L. P. Morin, K. M. Studholme, *J. Comp. Neurol.* **522**, 3733–3753 (2014).
4. E. H. Feinberg, M. Meister, *Nature* **519**, 229–232 (2015).
5. R. J. Cork, S. Z. Baber, R. R. Mize, *J. Comp. Neurol.* **394**, 205–217 (1998).
6. R. R. Mize, *Prog. Brain Res.* **112**, 35–55 (1996).
7. B. D. Corneil, D. P. Munoz, *Neuron* **82**, 1230–1243 (2014).
8. N. Sahibzada, P. Dean, P. Redgrave, *J. Neurosci.* **6**, 723–733 (1986).
9. P. Dean, P. Redgrave, G. W. Westby, *Trends Neurosci.* **12**, 137–147 (1989).
10. J. D. Cohen, M. A. Castro-Alamancos, *J. Neurosci.* **30**, 8502–8511 (2010).
11. J. T. DesJardin et al., *J. Neurosci.* **33**, 150–155 (2013).
12. F. Zhang et al., *Nat. Protoc.* **5**, 439–456 (2010).
13. J. P. Johansen, S. B. Wolff, A. Lüthi, J. E. LeDoux, *Biol. Psychiatry* **71**, 1053–1060 (2012).
14. Experimental procedures are explained in the supplementary materials on Science Online.
15. L. Madisen et al., *Nat. Neurosci.* **15**, 793–802 (2012).
16. S. Hippenmeyer et al., *PLOS Biol.* **3**, e159 (2005).
17. H. Taniguchi et al., *Neuron* **71**, 995–1013 (2011).
18. T. A. Münch et al., *Nat. Neurosci.* **12**, 1308–1316 (2009).
19. L. Madisen et al., *Nat. Neurosci.* **13**, 133–140 (2010).
20. V. F. Descalzo, L. G. Nowak, J. C. Brumberg, D. A. McCormick, M. V. Sanchez-Vives, *J. Neurophysiol.* **93**, 1111–1118 (2005).
21. Y. J. Liu, Q. Wang, B. Li, *Brain Behav. Evol.* **77**, 193–205 (2011).
22. M. Yilmaz, M. Meister, *Curr. Biol.* **23**, 2011–2015 (2013).
23. X. Zhao, M. Liu, J. Cang, *Neuron* **84**, 202–213 (2014).
24. P. Anikeeva et al., *Nat. Neurosci.* **15**, 163–170 (2012).
25. J. Y. Cohen, S. Haesler, L. Vong, B. B. Lowell, N. Uchida, *Nature* **482**, 85–88 (2012).
26. E. Comoli et al., *Front. Neuroanat.* **6**, 9 (2012).
27. W. Xu, T. C. Südhof, *Science* **339**, 1290–1295 (2013).
28. A. Pitkanen, V. Savander, J. E. LeDoux, *Trends Neurosci.* **20**, 517–523 (1997).
29. J. F. Medina, J. C. Repa, M. D. Mauk, J. E. LeDoux, *Nat. Rev. Neurosci.* **3**, 122–131 (2002).
30. A. S. Jansen, X. V. Nguyen, V. Karpitskiy, T. C. Mettenleiter, A. D. Loewy, *Science* **270**, 644–646 (1995).
31. T. Ono, P. G. Luiten, H. Nishijo, M. Fukuda, H. Nishino, *Neurosci. Res.* **2**, 221–238 (1985).
32. H. Hu, J. Gan, P. Jonas, *Science* **345**, 1255263 (2014).
33. H. Fotowat, F. Gabbiani, *Annu. Rev. Neurosci.* **34**, 1–19 (2011).

ACKNOWLEDGMENTS

We thank T. Südhof, K. Deisseroth, Y. Wang, B. Li, and M. Luo for providing plasmids, instruments, and technical support for this study. This work was supported by the Thousand Young Talents Program of China. We declare no conflicts of interest. All data are archived in the Institute of Biophysics, Chinese Academy of Sciences.

SUPPLEMENTARY MATERIALS

www.sciencemag.org/content/348/6242/1472/suppl/DC1
Materials and Methods
Supplementary Text
Figs. S1 to S12
Table S1 and S2
Reference (34)
Movies S1 to S5
Data S1

6 February 2015; accepted 28 May 2015
10.1126/science.aaa8694

STRUCTURAL BIOLOGY

A Cas9-guide RNA complex preorganized for target DNA recognition

Fuguo Jiang,¹ Kaihong Zhou,² Linlin Ma,² Saskia Gressel,³ Jennifer A. Doudna^{1,2,4,5,6,7*}

Bacterial adaptive immunity uses CRISPR (clustered regularly interspaced short palindromic repeats)–associated (Cas) proteins together with CRISPR transcripts for foreign DNA degradation. In type II CRISPR-Cas systems, activation of Cas9 endonuclease for DNA recognition upon guide RNA binding occurs by an unknown mechanism. Crystal structures of Cas9 bound to single-guide RNA reveal a conformation distinct from both the apo and DNA-bound states, in which the 10-nucleotide RNA “seed” sequence required for initial DNA interrogation is preordered in an A-form conformation. This segment of the guide RNA is essential for Cas9 to form a DNA recognition-competent structure that is poised to engage double-stranded DNA target sequences. We construe this as convergent evolution of a “seed” mechanism reminiscent of that used by Argonaute proteins during RNA interference in eukaryotes.

CRISPR-Cas proteins function in complex with mature CRISPR RNAs (crRNAs) to identify and cleave complementary target sequences in foreign nucleic acids (1). In type II CRISPR systems, the Cas9 enzyme cleaves DNA at sites defined by the 20-nucleotide (nt) guide segment within crRNAs, together with a trans-activating crRNA (tracrRNA) (2) that forms a crRNA:tracrRNA hybrid structure capable of Cas9 association (3). Once assembled on target DNA, the Cas9 HNH and RuvC nuclease domains cleave the double-stranded DNA (dsDNA) sequence within the strands that are complementary and noncomplementary to the guide RNA segment, respectively (3, 4) (Fig. 1A). By engineering a synthetic single-guide RNA (sgRNA) that fuses the crRNA and tracrRNA into a single transcript of 80 to 100 nt (Fig. 1B), Cas9:sgRNA has been harnessed as a two-component programmable system for genome engineering in various organisms (5, 6).

The utility of Cas9 for both bacterial immunity and genome engineering applications relies on accurate DNA target selection. Target choice relies on base pairing between the DNA and the 20-nt guide RNA sequence, as well as the presence of a 2- to 4-base pair (bp) protospacer adjacent motif (PAM) proximal to the target site (3, 4). The target complementarity of a “seed” sequence within the guide segment of crRNAs is critical for DNA recognition and cleavage (7, 8). In type II CRISPR systems, Cas9 binds to targets by recognizing a

PAM and searching the adjacent DNA for complementarity to the 10- to 12-nt “seed” sequence at the 3' end of the guide RNA segment (Fig. 1B) (3, 9–11). Crystal structures of Cas9 bound to sgRNA and a target DNA strand, with or without a partial PAM-containing nontarget strand, show the entire 20-nt guide RNA segment engaged in an A-form helical interaction with the target DNA strand (12, 13). How the “seed” region within the guide RNA specifies DNA binding has remained unknown.

To determine how Cas9 assembles with and positions the guide RNA prior to substrate recognition, we solved the crystal structure of catalytically active *Streptococcus pyogenes* Cas9 (SpyCas9) in complex with an 85-nt sgRNA at 2.9 Å resolution (Fig. 1 and table S1). The overall structure of the Cas9-sgRNA binary complex, representing the pre-target-bound state of the enzyme, resembles the bilobed architecture of the target DNA-bound state, as observed in electron microscopic studies (14), with the guide segment of the sgRNA positioned in the central channel between the nuclease and helical recognition lobes (Fig. 1, C to E). This structural architecture and guide RNA organization is maintained in the crystal structure of a widely used nuclease-inactive version of Cas9 (D10A/H840A, referred to as dCas9) in complex with sgRNA (fig. S1).

Comparison of SpyCas9 crystal structures representing the protein alone and the RNA-bound and RNA-DNA-bound states of the enzyme reveals the nature of Cas9's conformational flexibility during sgRNA binding and target DNA recognition (Fig. 2A and figs. S2 and S3). The helical recognition lobe undergoes substantial rearrangements upon sgRNA binding but before DNA association, especially in helical domain 3, which moves as a rigid body by ~65 Å into close proximity with the HNH domain (fig. S2D). Superposition of the Cas9-sgRNA pre-target-bound complex onto the target DNA-bound structures reveals further

¹Department of Molecular and Cell Biology, University of California, Berkeley, CA 94720, USA. ²Howard Hughes Medical Institute, University of California, Berkeley, CA 94720, USA. ³Max Planck Institute for Biophysical Chemistry, 37077 Göttingen, Germany. ⁴California Institute for Quantitative Biosciences, University of California, Berkeley, CA 94720, USA. ⁵Department of Chemistry, University of California, Berkeley, CA 94720, USA. ⁶Physical Biosciences Division, Lawrence Berkeley National Laboratory, Berkeley, CA 94720, USA. ⁷Innovative Genomics Initiative, University of California, Berkeley, CA 94720, USA.

*Corresponding author. E-mail: doudna@berkeley.edu

This copy is for your personal, non-commercial use only.

If you wish to distribute this article to others, you can order high-quality copies for your colleagues, clients, or customers by [clicking here](#).

Permission to republish or repurpose articles or portions of articles can be obtained by following the guidelines [here](#).

The following resources related to this article are available online at www.sciencemag.org (this information is current as of August 24, 2015):

Updated information and services, including high-resolution figures, can be found in the online version of this article at:

<http://www.sciencemag.org/content/348/6242/1472.full.html>

Supporting Online Material can be found at:

<http://www.sciencemag.org/content/suppl/2015/06/24/348.6242.1472.DC1.html>

This article **cites 33 articles**, 8 of which can be accessed free:

<http://www.sciencemag.org/content/348/6242/1472.full.html#ref-list-1>

This article appears in the following **subject collections**:

Neuroscience

<http://www.sciencemag.org/cgi/collection/neuroscience>